Photoluminescence and photothermal effect of Fe3O4 nanoparticles for medical imaging and therapy

M. E. Sadat, Masoud Kaveh Baghbador, Andrew W. Dunn, H. P. Wagner, Rodney C. Ewing, Jiaming Zhang, Hong Xu, Giovanni M. Pauletti, David B. Mast, and Donglu Shi

Articles you may be interested in

Facile functionalization of Fe2O3 nanoparticles to induce inherent photoluminescence and excellent photocatalytic activity
Appl. Phys. Lett. **104**, 233110 (2014); 10.1063/1.4882904

Particle size dependence of heating power in MgFe2O4 nanoparticles for hyperthermia therapy application
J. Appl. Phys. **115**, 17B522 (2014); 10.1063/1.4867751

Effects of core/shell structure on magnetic induction heating promotion in Fe3O4/-Fe2O3 magnetic nanoparticles for hyperthermia
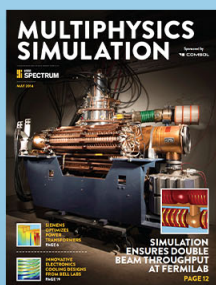Appl. Phys. Lett. **103**, 163104 (2013); 10.1063/1.4825270

Fe3O4-nanoparticles within porous silicon: Magnetic and cytotoxicity characterization
Appl. Phys. Lett. **102**, 193110 (2013); 10.1063/1.4807421

Physical limits of pure superparamagnetic Fe3O4 nanoparticles for a local hyperthermia agent in nanomedicine
Appl. Phys. Lett. **100**, 092406 (2012); 10.1063/1.3689751

Photoluminescence and photothermal effect of Fe$_3$O$_4$ nanoparticles for medical imaging and therapy

M. E. Sadat,[1] Masoud Kaveh Baghbador,[1] Andrew W. Dunn,[2] H. P. Wagner,[1] Rodney C. Ewing,[3] Jiaming Zhang,[3] Hong Xu,[4] Giovanni M. Pauletti,[5] David B. Mast,[1,a] and Donglu Shi[2,6,a]

[1]*Department of Physics, University of Cincinnati, Cincinnati, Ohio 45221, USA*
[2]*The Materials Science and Engineering Program, Department of Mechanical and Materials Engineering, College of Engineering and Applied Science, University of Cincinnati, Cincinnati, Ohio 45221, USA*
[3]*Department of Geological and Environmental Sciences, Stanford University, Stanford, California 94305-2115, USA*
[4]*Med-X Institute, Shanghai Jiao Tong University, Shanghai 200030, People's Republic of China*
[5]*James L. Winkle College of Pharmacy, University of Cincinnati, Cincinnati, Ohio 45267, USA*
[6]*Shanghai East Hospital, The Institute for Biomedical Engineering & Nano Science, Tongji University School of Medicine, Shanghai 200120, People's Republic of China*

Photoluminescence (PL) of Fe$_3$O$_4$ nanoparticle was observed from the visible to near-infrared (NIR) range by laser irradiation at 407 nm. PL spectra of ∼10 nm diameter Fe$_3$O$_4$ nanoparticles organized in different spatial configuration, showed characteristic emissions with a major peak near 560 nm, and two weak peaks near 690 nm and 840 nm. Different band gap energies were determined for these Fe$_3$O$_4$ nanoparticle samples corresponding to, respectively, the electron band structures of the octahedral site (2.2 eV) and the tetrahedral site (0.9 eV). Photothermal effect of Fe$_3$O$_4$ nanoparticles was found to be associated with the photoluminescence emissions in the NIR range. Also discussed is the mechanism responsible for the photothermal effect of Fe$_3$O$_4$ nanoparticles in medical therapy. © 2014 AIP Publishing LLC. [http://dx.doi.org/10.1063/1.4895133]

Photoluminescence (PL) is not only a phenomenon of light emission from bulk materials, but has been recently discovered as a characteristic in many nanoparticle systems including quantum dots,[1] Si,[2] gold,[3] and zinc-blend quantum rods.[4] While the PL of these materials involve light emissions from visible to near infrared, the undergoing excitation mechanisms can range from bound excitons in quantum dots to surface plasmon in metal nanoparticles. The interband defect states and/or quantum confinement also play important roles in porous nanoparticles of Si.[5] Recent studies have been focused on Fe$_3$O$_4$ of various forms for both fundamental studies and medical applications.[6] However, photoluminescence of Fe$_3$O$_4$ has not been reported, neither as a bulk property nor in the nanoscale nanoparticles. In this study, we report on the photoluminescence/fluorescence properties of colloidal Fe$_3$O$_4$ over a wide range of particle sizes (10 nm–5 μm). These properties have important applications in early cancer diagnosis,[7] *in-vivo* imaging,[8] and photothermal threapy.[9] The PL spectra are consistent with the electronic bands that are associated with the structure of Fe$_3$O$_4$. We also identify the mechanism of the photothermal effect of Fe$_3$O$_4$ nanoparticles in terms of PL emission in the near infrared (NIR) region.

The photoluminescence measurements were performed on two distinctively different Fe$_3$O$_4$ nanoparticle systems. The preparation methods to synthesize poly(acrylic acid) (PAA)/Fe$_3$O$_4$, PS/Fe$_3$O$_4$, and Si/PS/Fe$_3$O$_4$ are described in our previous reports.[10,11] In one system, the Fe$_3$O$_4$ nanoparticles had an average diameter of 10 nm and were surface functionalized with poly(acrylic acid), denoted as PAA/Fe$_3$O$_4$. In the second system, the similar Fe$_3$O$_4$ nanoparticles were embedded in polystyrene matrix spheres with an average diameter of 100 nm. The average diameter of 10 nm was confirmed by transmission electron microscopy (TEM) of the PAA/Fe$_3$O$_4$ nanoparticles [Fig. 1(a)]. In previous studies, we have shown that these particles are superparamagnetic with reversible magnetic hysteresis curves.[12,13] TEM images of the Fe$_3$O$_4$ nanoparticles embedded in the matrix of the polystyrene spheres (PS/Fe$_3$O$_4$) with an average diameter of 100 nm are shown in Fig. 1(b). For medical applications, the PS/Fe$_3$O$_4$ was coated with a thin silica film (Si/PS/Fe$_3$O$_4$) as a functional group for conjugation of various biological molecules [Fig. 1(c)], with the similar size and morphology as the PS/Fe$_3$O$_4$. The hydrodynamic diameters and size distributions of PAA/Fe$_3$O$_4$, PS/Fe$_3$O$_4$, and Si/PS/Fe$_3$O$_4$ dispersed in water were determined by Zetasizer Nano Series, Malvern Instruments.[24]

A schematic of the photoluminescence measurement is shown in Fig. 2(a). Fig. 2(b) shows the PL spectra of the PAA/Fe$_3$O$_4$, PS/Fe$_3$O$_4$, and Si/PS/Fe$_3$O$_4$ measured at 10 mg/ml with a solid state laser of 4.5 mW and excitation wavelength 407 nm (3.04 eV). All of the spectra show multiple peaks in the scan range from 465 nm to 900 nm. We assumed Gaussian distribution a good fit to the experimental PL data for all three peaks. The most intensive peak observed for PAA/Fe$_3$O$_4$ occurs at ∼540 nm (2.296 eV) while those for the PS/Fe$_3$O$_4$ and Si/PS/Fe$_3$O$_4$ are at ∼565 nm (2.194 eV). Thus, there appears a blue shift of the PL peak for PAA/Fe$_3$O$_4$ that can be attributed to quantum confinement. The average diameter of PAA/Fe$_3$O$_4$ is approximately 10 nm, while PS/Fe$_3$O$_4$ and Si/PS/Fe$_3$O$_4$ consist of large Fe$_3$O$_4$

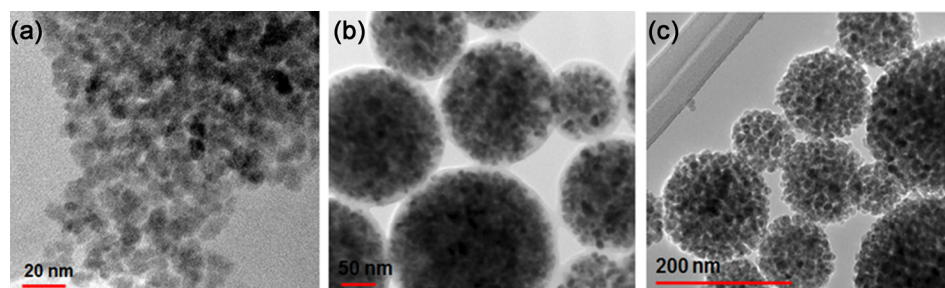a)Authors to whom correspondence should be addressed. Electronic mail: mastdb@ucmail.uc.edu and donglu.shi@uc.edu

FIG. 1. (a) The TEM image of PAA/Fe_3O_4 shows the monodispersed nanoparticles with an average 10 nm in diameter. The TEM images of (b) PS/Fe_3O_4 and Si/PS/Fe_3O_4 (c) show the 10 nm diameter nanoparticles embedded in the polystyrene matrices of 100 nm. A thin layer of silica coating can be seen on the surfaces of Si/PS/Fe_3O_4.
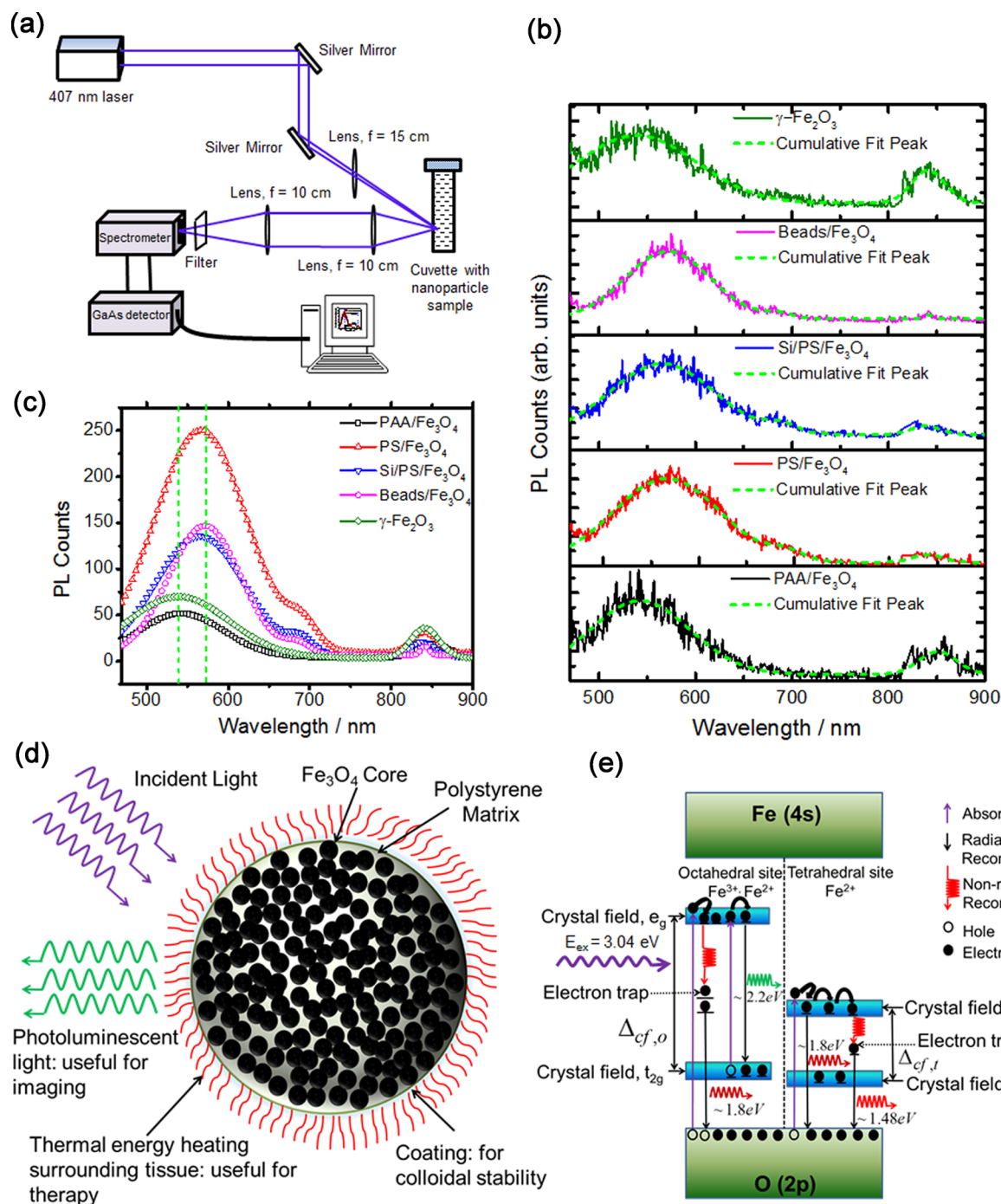

FIG. 2. (a) Schematic of the experimental set up for the photoluminescence measurement. (b) Photoluminescence spectra of the samples indicated, where solid lines are experimental spectra, and the cumulative peak fit of the Gaussian curves are shown as the dashed lines. (c) Cumulative fit peak of the PL spectra of the samples indicated; the vertical dashed lines show the blue shift of PAA/Fe_3O_4 and γ-Fe_2O_3 with respect to the 5 μm Fe_3O_4 beads. The PL counts of PS/Fe_3O_4, Si/PS/Fe_3O_4, and Beads/Fe_3O_4 are seen to be much higher compared to those of PAA/Fe_3O_4 and γ-Fe_2O_3. (d) The schematic showing the spatially confined Fe_3O_4 nanoparticles embedded in the spherical polystyrene matrix in samples of PS/Fe_3O_4 and Si/PS/Fe_3O_4. (e) Schematic of the energy bands of the Fe_3O_4 nanoparticle system.

clusters on the order of $\sim$100 nm. The fluorescence spectra (measured with Hitachi, F-2500 spectrophotometer with 350 nm excitation) and images (taken with Zeiss LSM 710 confocal microscope with 488 nm excitation) of these magnetic nanoparticles are found to be consistent with the PL measurements.[24]

In order investigate the size dependence, the PL measurements were carried out on the 5 μ m BcMag^{TM} carboxyl-terminated magnetite beads (Beads/Fe$_3$O$_4$). For the structural effect on PL, the same experiments were performed on γ-Fe$_2$O$_3$ nanoparticles of 20 nm, dispersed in water. The major peak is further red-shifted to $\sim$571 nm (2.171 eV) for the 5 μ m magnetite beads and blue-shifted to $\sim$540 nm for the γ-Fe$_2$O$_3$ nanoparticles [Fig. 2(b)]. The shift in energy is 0.125 eV between the 10 nm diameter PAA/Fe$_3$O$_4$ nanoparticles and 5 μ m magnetite beads. These results are consistent with a blue shift of 0.136 eV reported by Susamu *et al.*, where they showed an absorption peak at 0.886 eV in the 7 nm diameter magnetite particles compared with that of its bulk counterpart (600 nm thin film) due to quantum confinement.[14]

For direct comparison of different samples, PL counts are plotted as a function of wavelength for each sample as shown in Fig. 2(c). The peak counts near 540 nm for both PAA/Fe$_3$O$_4$ and γ-Fe$_2$O$_3$ are much less as compared with those of PS/Fe$_3$O$_4$, Si/PS/Fe$_3$O$_4$, and Beads/Fe$_3$O$_4$. These differences in intensity can be attributed to the collective emissions of large clusters of nanoparticles confined in the polystyrene matrices in PS/Fe$_3$O$_4$ and Si/PS/Fe$_3$O$_4$, giving rise to much higher PL counts. For PAA/Fe$_3$O$_4$, well-dispersed nanoparticles (10 nm) in colloids may only emit light individually, resulting in much weaker PL counts. Furthermore, well-dispersed PAA/Fe$_3$O$_4$ nanoparticles may also result in high scattering of the incident and emission lights, leading to a considerably reduced emission intensity. This situation is improved in the PS/Fe$_3$O$_4$ and Si/PS/Fe$_3$O$_4$ as they may be viewed as larger clusters (i.e., fewer scatterers). For power dependence, the PL measurements were carried out using a 1.5 mW laser, and the results show characteristics similar to those described above.[24]

Nanoparticles have very large surface areas (or a high density of defects on the surface). Typically, PL has a reduced intensity with broadening of the emission peaks as a result of these nanoparticle defects. The effect of the surface defects on the electronic structure can lead to narrowing of the band gap. In this case, electrons can non-radiatively move between the different defect sites by releasing thermal energy. For all samples in this study, peaks at $\sim$690 nm and $\sim$840 nm can be attributed to the transitions of trapped electrons from different defect sites. Mercado *et al.* showed much higher PL intensity from a dense film of nanocrystalline titanium dioxide (TiO$_2$) as compared with its porous counterpart. They attributed this difference to the presence of oxygen vacancies for which the O$_2$ binding site is less accessible in the dense film.[15] Sefatting *et al.* have shown a PL intensity increase for the transition metal dichalcogenides (MoS$_2$, MoSe$_2$, WSe$_2$) with increasing defect densities.[16] Also reported by Arras *et al.*, defects in Fe$_3$O$_4$ can lead to the formation of oxygen vacancies that can modify the electronic band structure.[17]

A schematic diagram representing the spatial arrangement of the Fe$_3$O$_4$ nanoparticles in PS/Fe$_3$O$_4$ and Si/PS/

Fe$_3$O$_4$ is shown in Fig. 2(d). In contrast to PAA/Fe$_3$O$_4$, where the nanoparticles are well dispersed in the liquid, the Fe$_3$O$_4$ nanoparticles are rigidly confined in a spherical polymer matrix in PS/Fe$_3$O$_4$ and Si/PS/Fe$_3$O$_4$. Bulk magnetite (Fe$_3$O$_4$) has an inverse spinel structure, which consists of face-centered-cubic lattice of O^{2-} ions where the tetrahedral site is occupied by Fe^{3+} and approximately equal numbers of Fe^{3+} and Fe^{2+} ions occupy the octahedral site according to the chemical formula (Fe^{3+})[Fe^{3+}Fe^{2+}](O^2)$_4$.[18] Several studies have shown that the valence band of the O(2p) to the empty Fe(4s) in Fe$_3$O$_4$ is separated by 4–6 eV.[19] Between these bands are the crystal field bands of the octahedral and tetrahedral sites that are composed of 3d metal atomic orbital. Fig. 2(e) shows the approximate band structures of the Fe$_3$O$_4$ nanoparticles, as estimated by our photoluminescence measurements. Several previous experimental measurements and theoretical calculations have reported that the energy gap due to crystal-field splitting on the octahedral site is $\Delta_{cf,o} \sim 2.2$ eV, while that of the tetrahedral site is $\Delta_{cf,t} \sim 0.9$ eV. The valence band of O(2p) is further separated from crystal field site t_{2g}, e of the octahedral and tetrahedral site, respectively, by almost ~ 0.9 eV.[20–22] Thus, upon excitation by an energy of 3.04 eV (407 nm) on Fe$_3$O$_4$, electron transfer from the valence band O(2p) to the crystal field (e_g) on the octahedral site requires an energy of 3.1 eV. The electron can also make a transition from $t_{2g} \rightarrow e_g$ (2.2 eV) on the octahedral site, $e \rightarrow t_2$ (0.9 eV) on the tetrahedral site, and $O(2p) \rightarrow t_2$ (1.8 eV) on the tetrahedral site.

Based on the model proposed in Fig. 2(e), the PL peak at $\sim$565 nm (2.2 eV) can be attributed to the radiative recombination of mobile electrons from $e_g \rightarrow t_{2g}$ on the octahedral site, and the peak at $\sim$690 nm (1.79 eV), the recombination of trapped electrons on the octahedral site to O(2p), or recombination of mobile electrons in the crystal field (t_2) of tetrahedral site to O(2p). The peaks at 565 nm and 690 nm are consistent with the energy gaps caused by crystal-field splitting of the octahedral site and the energy difference between O(2p) and t_2 of the tetrahedral site. A near-infrared peak is observed at $\sim$840 nm (1.47 eV), which can be attributed to the electron traps on the tetrahedral site, that are associated with the oxygen vacancies. These structural characteristics are consistent with the electronic band structures of Fe$_3$O$_4$ as described above.

In order to investigate the optical absorption properties of the materials, UV-VIS-NIR absorption spectra of the Fe$_3$O$_4$ nanoparticle samples were measured by using a spectrophotometer (Hitachi U- 3010) from wavelength range of 300 nm to 950 nm. Fig. 3(a) shows the absorption co-efficient (α) as a function of photon energy (E) for all three samples at the concentration of 1 mg/ml. The absorption co-efficient (α) obeys the following relation at a given temperature (T):

$$\alpha = \alpha_0 \exp\left[\sigma \left(\frac{E - E_0)}{k_B T} \right) \right], \qquad (1)$$

where α_0 is the absorption coefficient, E is the incident energy, E_o is the onset of absorption, and $E_u = \frac{k_B T}{\sigma}$ is the Urbach energy, where σ is the steepness parameter and k_B is the Boltzmann constant. Urbach energy is a measure of defect density in the crystal that originates from thermal
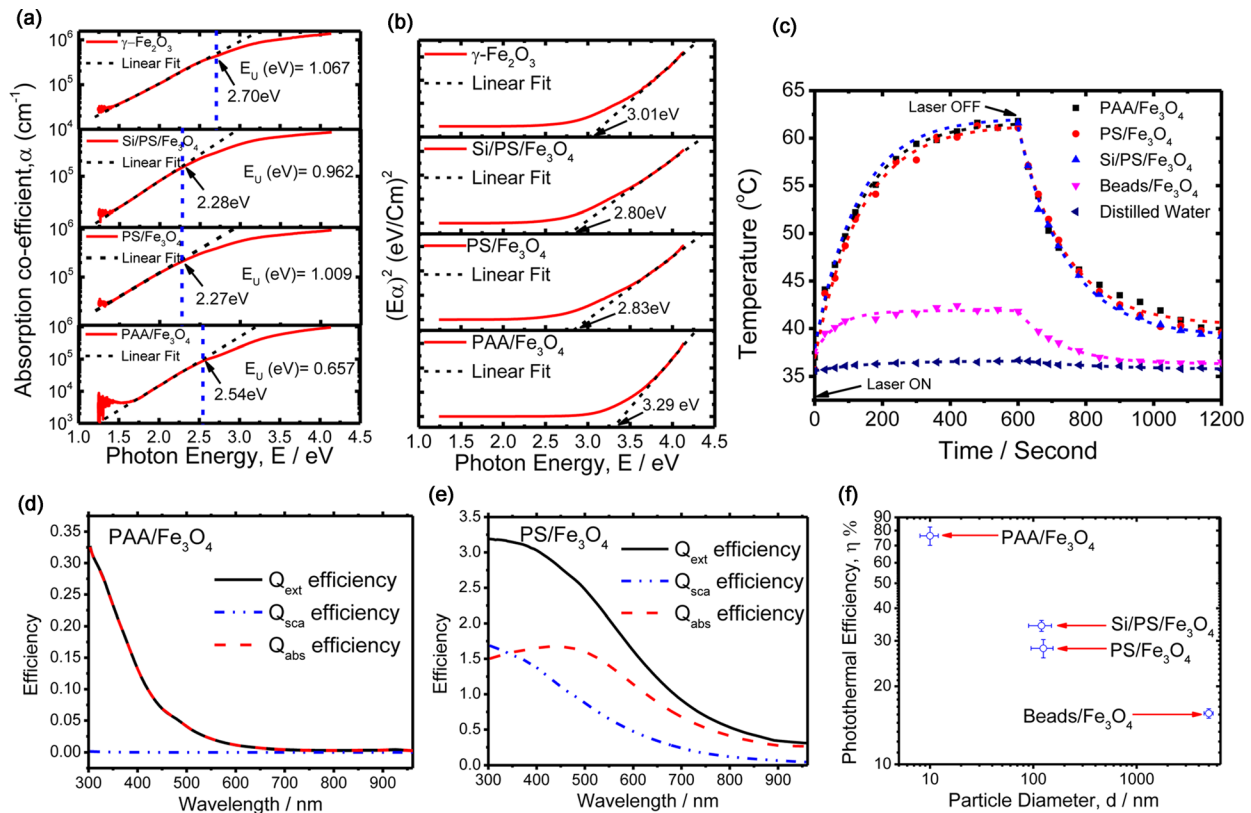
FIG. 3. (a) UV-VIS-NIR absorbance spectra of the Fe_3O_4 nanoparticle samples in colloidal solution. The y-axis is plotted in logarithmic scale; the solid line represents the experimental absorption spectra, and dashed line—the fit to the linear portion of the curve; and the Urbach energy and onset of absorption are determined by the fitting. (b) Plot of $(E\alpha)^2$ vs. photon energy, where solid line represents the experimental absorption curve, and dashed line—the fit to the linear portion of the data, where the intercept of that curve in the x-axis gives the estimation of direct band gap. (c) Heating and cooling curves of the Fe_3O_4 nanoparticle samples illuminated with 808 nm light (laser power = 0.841 W, beam diameter = 1 cm). (d) and (e) Extinction (Q_{ext}), absorption (Q_{abs}), scattering (Q_{sca}) efficiencies as a function of wavelength for PAA/Fe_3O_4 and PS/Fe_3O_4, respectively. The values are calculated by the Mie theory using the complex refractive indices of the samples. (f) Photothermal transduction efficiency as a function of particle diameter in logarithmic scale. The horizontal error bar represents the particle size distribution, and the vertical error bars indicate the standard error of photothermal efficiency.

fluctuations, impurities, and disorder.[23] By plotting the absorption coefficient on a logarithmic scale as a function of photon energy, the Urbach energy is obtained from the linear portion of the curve. One can also see that [Fig. 3(a)] the onset of absorption (E_o) is a close match with the crystal-field splitting energy of the octahedral site. The direct band gap value is also estimated by plotting $(E\alpha)^2$ as a function of photon energy [Fig. 3(b)], where extrapolation of the linear portion of the curve to the x axis gives the value of the direct band gap. The values are consistent with the energy difference ($\sim$3.1 eV) between O(2p) and (e_g) of the octahedral site.

In order to determine the photothermal transduction efficiency of each nanoparticle solution, a fiber-coupled continuous wave diode-laser of wavelengths 808 nm was used to irradiate the sample of 200 μl and at 1 mg/ml concentrations. Fig. 3(c) shows the time vs. temperature curves for all samples irradiated with NIR light (808 nm) at a power density of 1.07 W/cm^2. A schematic of the experimental set up and thermal images of the Fe_3O_4 nanoparticles measured with another diode laser of wavelength 785 nm and intensity 0.998 W/cm^2 is shown in the supplementary material.[24] The photothermal transduction efficiency was calculated from the cooling rate using the following equation:

$$\eta = \frac{hA(T_{max} - T_{min}) - E_{in,sample}}{I(1 - 10^{-OD})}, \quad (2)$$

where, h is the heat transfer coefficient, A is the sample well surface area, T_{max} is the maximum temperature of the nanoparticle solutions after 10 min of laser exposure, T_{min} is the surface temperature of the hot plate, $E_{in,sample}$ is the energy input based on the heat generated by solvent and sample well, I is the laser power in watt, OD is the optical density, and the product of hA can be calculated from the decay time constant, $t = mC_p/hA$, where m and C_p are the mass and heat capacity of the solvent, respectively. The theoretical efficiency which is the ratio of absorption efficiency (Q_{abs}) to extinction efficiency (Q_{ext}) was calculated by using the complex refractive index ($n = n' + ik$) of each sample, where n' denotes the real refractive index and k is the imaginary part of the refractive index. The real part of the refractive index is calculated for each wavelength by numerically integrating the experimental absorbance data using the kramers-kronig relation.[24] Figs. 3(d)–3(e) show the extinction efficiency (Q_{ext}), absorption efficiency (Q_{abs}), and scattering efficiency (Q_{sca}) as a function of wavelength for PAA/Fe_3O_4 and PS/Fe_3O_4. As can be seen from Fig. 3(d), the extinction efficiency of PAA/Fe_3O_4 calculated by the Mie theory is mostly absorption dominated, while that of PS/Fe_3O_4 is not [Fig. 3(e)]. Both PS/Fe_3O_4 and Si/PS/Fe_3O_4 have lower Q_{abs}/Q_{ext} ratios (0.774 and 0.900, respectively) at 808 nm compared to PAA/Fe_3O_4 (1.00), as well as less efficient photothermal performance. Fig. 3(f)

shows that smaller nanoparticles (PAA/Fe_3O_4) exhibit much higher photothermal heating efficiency (76%) as compared with PS/Fe_3O_4 (28%), Si/PS/Fe_3O_4 (34%), and beads/Fe_3O_4 (16%). This is consistent with the fact that the smaller particles with higher surface area exhibit more efficient photothermal heating. At the same time, however, smaller particles result in lower PL emission indicating dominant phonon-mediated, non-radiative transition.

In summary, photoluminescence was observed in Fe_3O_4 over a wide range of particle sizes (10 nm–5 μ m). Due to the different spatial arrangements and confinement geometries of the nanoparticles, Fe_3O_4 may exhibit PL from the visible to the near-infrared region, although with varied intensities and wavelengths. A blue-shift was observed for PAA/Fe_3O_4 due to quantum confinement. Much higher PL intensities were observed for the PS/Fe_3O_4 and Si/PS/Fe_3O_4 due to collective emissions and reduced light-scattering. Band gap energies were determined based on the PL spectra that correspond to the electronic structures of the octahedral site (2.2 eV) and the tetrahedral site (1.8 eV). The mechanism of the Fe_3O_4 photothermal behavior was determined based on the PL emission in the NIR region. Thus, the photothermal hyperthermia of Fe_3O_4 nanoparticles can be utilized as an effective therapeutic means for highly localized treatment of cancers.

[1]J.-Y. Marzin, J.-M. Gérard, A. Izrael, D. Barrier, and G. Bastard, Phys. Rev. Lett. **73**, 716 (1994).

[2]W. D. A. M. De Boer, D. Timmerman, K. Dohnalova, I. N. Yassievich, H. Zhang, W. J. Buma, and T. Gregorkiewicz, Nat. Nanotechnol. **5**, 878 (2010).

[3]A. Bouhelier, R. Bachelot, G. Lerondel, S. Kostcheev, P. Royer, and G. P. Wiederrecht, Phys. Rev. Lett. **95**, 267405 (2005).

[4]S. Kan, T. Mokari, E. Rothenberg, and U. Banin, Nat. Mater. **2**, 155 (2003).

[5]S. Godefroo, M. Hayne, M. Jivanescu, A. Stesmans, M. Zacharias, O. I. Lebedev, G. Van Tendeloo, and V. V. Moshchalkov, Nat. Nanotechnol. **3**, 174 (2008).

[6]A. K. Gupta, R. R. Naregalkar, V. D. Vaidya, and M. Gupta, Nanomedicine **2**, 23–29 (2007).

[7]F. Q. Hu, L. Wei, Z. Zhou, Y. L. Ran, Z. Li, and M. Y. Gao, Adv. Mater. **18**, 2553 (2006).

[8]L. Wang, K. G. Neoh, E. T. Kang, B. Shuter, and S. C. Wang, Adv. Funct. Mater. **19**, 2615 (2009).

[9]M. Chu, Y. Shao, J. Peng, X. Dai, H. Li, Q. Wu, and D. Shi, Biomaterials **34**, 4078 (2013).

[10]F. Xu, C. Cheng, D. X. Chen, and H. Gu, ChemPhysChem **13**, 336 (2012).

[11]H. Xu, L. Cui, N. Tong, and H. Gu, J. Am. Chem. Soc. **128**, 15582 (2006).

[12]M. E. Sadat, R. Patel, J. Sookoor, S. L. Bud'ko, R. C. Ewing, J. Zhang, H. Xu, Y. Wang, G. M. Pauletti, D. B. Mast, and D. Shi, Mater. Sci. Eng. C **42**, 52 (2014).

[13]M. E. Sadat, R. Patel, R. C. Ewing, J. Zhang, H. Xu, D. B. Mast, and D. Shi, Mater Lett **129**, 57 (2014).

[14]S. Taketomi, H. Takahashi, N. Inaba, and H. Miyajima, J. Phys. Soc. Jpn. **60**, 3426 (1991).

[15]C. Mercado, Z. Seeley, A. Bandyopadhyay, S. Bose, and J. L. McHale, ACS Appl. Mater. Interfaces **3**, 2281 (2011).

[16]S. Tongay, J. Suh, C. Ataca, W. Fan, A. Luce, J. S. Kang, J. Liu, C. Ko, R. Raghunathanan, and J. Zhou, Sci. Rep. **3**, 2657 (2013).

[17]R. Arras, L. Calmels, and B. Warot-Fonrose, Appl. Phys. Lett. **100**, 032403 (2012).

[18]W. F. J. Fontijn, P. J. Van der Zaag, M. A. C. Devillers, V. A. M. Brabers, and R. Metselaar, Phys. Rev. B **56**, 5432 (1997).

[19]J. Zaanen, G. A. Sawatzky, and J. W. Allen, Phys. Rev. Lett. **55**, 418 (1985).

[20]C. Boxall, G. Kelsall, and Z. Zhang, J. Chem. Soc., Faraday Trans. **92**, 791 (1996).

[21]W. F. J. Fontijn, P. J. Van der Zaag, L. F. Feiner, R. Metselaar, and M. A. C. Devillers, J. Appl. Phys. **85**, 5100 (1999).

[22]I. Balberg and H. L. Pinch, J. Magn. Magn. Mater. **7**, 12 (1978).

[23]S. M. Wasim, C. Rincon, G. Marin, P. Bocaranda, E. Hernández, I. Bonalde, and E. Medina, Phys. Rev. B **64**, 195101 (2001).

[24]See supplementary material at http://dx.doi.org/10.1063/1.4895133 for nanoparticle characterization information and analysis.